

A DISK-WIND DRIVING THE ROTATING MOLECULAR OUTFLOW IN CB 26

J. A. LÓPEZ-VÁZQUEZ^{1,2}, LUIS A. ZAPATA², AND CHIN-FEI LEE¹

¹Academia Sinica Institute of Astronomy and Astrophysics, No. 1, Sec. 4, Roosevelt Road, Taipei 10617, Taiwan

²Instituto de Radioastronomía y Astrofísica, Universidad Nacional Autónoma de México, Apartado Postal 3-72, 58089 Morelia, Michoacán, México

ABSTRACT

We present ¹²CO (J=2–1) sensitive molecular line and 1.3 mm continuum observations made with the Submillimeter Array (SMA) of the bipolar outflow associated with the young star located in the Bok globule known as CB 26. The SMA observations were carried out in its extended configuration allowing us to study the kinematics and structure of the outflow with about 1'' or 140 au resolution. We find that the dusty and edge-on circumstellar disk related with the outflow has an projected spatial (deconvolved) size of 196 ± 31 au \times 42 ± 29 au with a total (gas+dust) mass of 0.031 ± 0.015 M_⊙. We estimated a dynamical mass for the central object of 0.66 ± 0.03 M_⊙, and the mass of the molecular outflow of $5 \pm 1.5 \times 10^{-5}$ M_⊙. All these values are consistent with recent estimations. The observations confirm that the outflow rotation has a similar orientation to that of the edge-on disk. For the outflow, we find that the following quantities: the rotation velocity (~ 1 – 3 km s^{−1}), the specific angular momentum (~ 200 – 700 au km s^{−1}), and the launching radius (~ 15 – 35 au), decrease with the height above mid-plane, as observed in other molecular rotating outflows. The radius (~ 180 – 280 au), and expansion velocity (~ 2 – 4 km s^{−1}) also increase with the height above the disk mid-plane for $z < 0$ au, however, for $z > 0$ au these quantities do not present this behavior. Estimations for the outflow linear momentum rate, the outflow angular momentum rate, and the accretion luminosity seem to be well explained by a disk-wind present in CB26.

Keywords: ISM: jets and outflows – stars: individual (CB 26) – stars: pre-main sequence

1. INTRODUCTION

Rotating molecular outflows and protostellar jets are present in the early phases of the star formation process. They are thought to play an essential role in reducing the angular momentum from the disk-protostellar system (e.g., Blandford & Payne 1982 and Machida 2014) since it is proposed that these objects are ejected directly from the accretion disks (e.g., Pudritz & Norman 1986 and Bai et al. 2016). The molecular outflows in addition limit the mass of the star-disk system (Shu et al. 1993), and can induce changes in the chemical composition of their host cloud (e.g., Bachiller 1996), it is because some authors have proposed that the molecular outflows are a mixture between the entrained material of the molecular cloud and a stellar or disk wind (e.g., Shu et al. 1991 and López-Vázquez et al. 2019). Moreover, the protostellar jets could be helpful in the determination of the initial environmental properties related with planetary formation, given that these objects are able to remove the angular momentum of the material in the disk, allowing a continuous accretion towards the star. This is possible because planet formation begins much earlier than previously expected (Ray & Ferreira 2021).

Independent of their origin, it is expected that the molecular outflows present rotation signatures because they should inherit an angular momentum component from the accretion disk, or the parent cloud, or a combination of both. Recent studies have reported the rotation signatures in several sources, the molecular outflows with rotation are: CB 26 (Launhardt et al. 2009), Ori-S6 (Zapata et al. 2010), HH 797 (Pech et al. 2012), DG Tau B (Zapata et al. 2015 and de Valon et al. 2020), TMC1A (Bjerkeli et al. 2016), Orion Source I (Hirota et al. 2017 and López-Vázquez et al. 2020), HH 112 (Lee et al. 2018) HH 30 (Louvet et al. 2018), NGC 1333 IRAS 4C (Zhang et al. 2018), and HD 163296 (Booth et al. 2021). While, the protostellar jets with rotation are: HH 211 (Lee et al. 2009), HH 112 (Lee et al. 2017), and OMC 2/FIR 6b (Matsushita et al. 2021).

Located at 10° north of the Taurus Auriga dark cloud at a distance of 140 ± 20 pc (Launhardt et al. 2009), CB 26 is a Class I young stellar object (Stecklum et al. 2004) with a dynamical mass of the central star of $M_* = 0.55 \pm 0.1$ M_⊙, and an estimated age of about 1 Myr (Zhang et al. 2021). The central star has a luminosity $L_* \geq 0.5$ L_⊙ (Stecklum et al. 2004). The molecular outflow associated

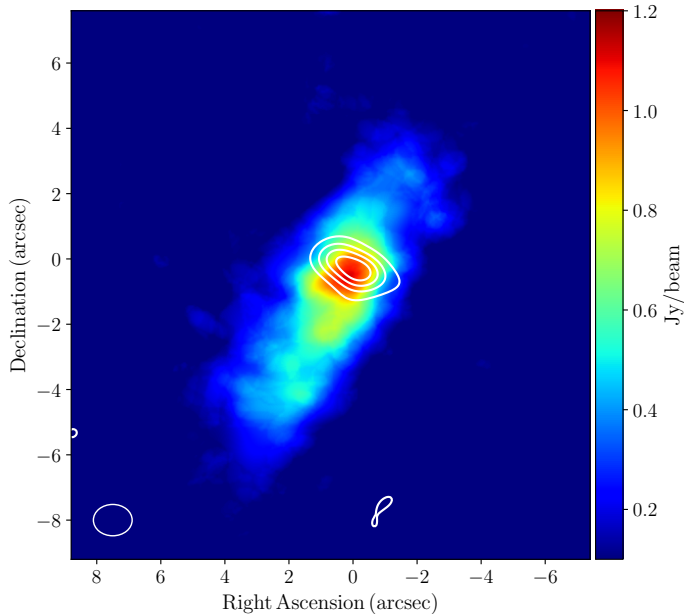


Figure 1. Moment zero of the ^{12}CO ($J=2-1$) emission line from the molecular outflow. The color scale bar on the right side shows the intensity in Jy/beam. The synthesized beam of the image is shown in the lower left corner. The white contours show the continuum emission from the disk and are the 16.5 mJy, 33.0 mJy, 49.5 mJy, and 66.0 mJy.

with CB 26 has an outward velocity of $\sim 10-12 \text{ km s}^{-1}$ along the southwest-northeast direction (Pety et al. 2006 and Launhardt et al. 2009), with a diameter of 2000 AU (Launhardt et al. 2009).

We present new ^{12}CO ($J=2-1$) molecular line observations, made with the Submillimeter Array (SMA) of the molecular outflow associated with the young star CB 26. This paper is organized in the following way: Section 2 details the observations. In Section 3 we present the results. In Section 4 we discuss our results. Finally, the conclusions are presented in Section 5.

2. OBSERVATIONS

The Submillimeter Array¹ observations of CB26 were carried out on October 4 2013 when the array was in its extended configuration. The baselines in this configuration ranged from 15 to 148 k λ . The phase center in the sky was centered to $\alpha_{J2000.0} = 04^{\text{h}}59^{\text{m}}50^{\text{s}}.7$, and $\delta_{J2000.0} = +52^{\circ}04'43''.6$ with a total integration time on source of 240 min. The Full Width Half Maximum (FWHM) of the primary beam is $57''$ at this frequency, so that the bulk of the molecular and dusty material associated with CB26 is well-covered, see Launhardt et al. (2009).

¹ The Submillimeter Array is a joint project between the Smithsonian Astrophysical Observatory and the Academia Sinica Institute of Astronomy and Astrophysics, and is funded by the Smithsonian Institution and the Academia Sinica.

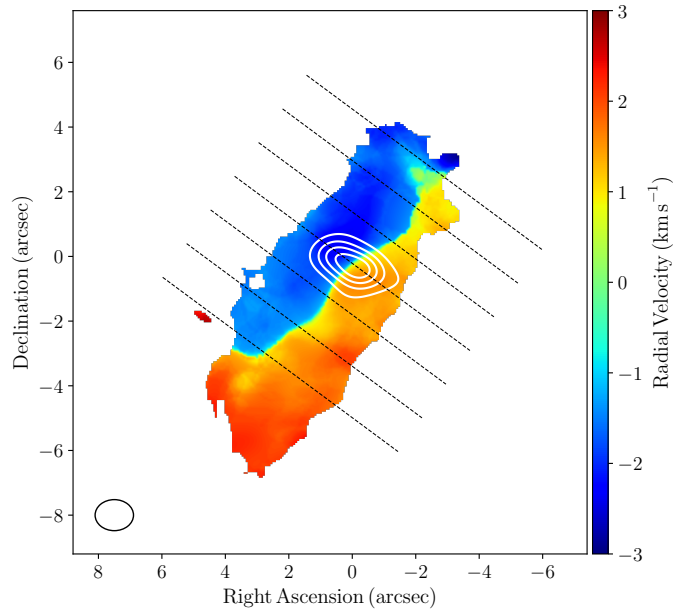


Figure 2. First moment or the intensity weighted velocity of the ^{12}CO ($J=2-1$) emission line from the molecular outflow. The diagonal dashed lines indicate the positions where the position-velocity diagrams were made (see Figure 3). The color scale bar on the right side shows the V_{LSR} in km s^{-1} . The synthesized beam of the image is shown in the lower left corner. The white contours show the continuum emission from the disk and are the 16.5 mJy, 33.0 mJy, 49.5 mJy, and 66.0 mJy.

Two frequency bands were observed simultaneously centered at 230.457 GHz (upper sideband) and 220.457 GHz (lower sideband). The SMA-SWARM correlator was configured to cover 2 GHz bandwidth in both bands. The native spectral resolution is 140 kHz per channel across the entire spectral band. This provided a velocity resolution of about 0.18 km s^{-1} . This spectral resolution is bit smaller to that obtained in Launhardt et al. (2009), 0.25 km s^{-1} . This very high spectral resolution allowed a reliable study of the CO kinematics in CB26 outflow.

With an average system temperature of about 150 K and with opacity at 225 GHz around 0.12, the observations were made in optimal conditions. Observations of Neptune and Uranus served for the flux density calibration. The gain calibrators were the quasars 3C 111 and J0533+483, while 3C454.3 was used for bandpass calibration. The estimated uncertainty in the flux scale, what is based in SMA monitoring, is in a window between 15% to 20%.

The IDL superset MIR developed for the Owens Valley Radio Observatory and adapted for the SMA² was used for the calibration of the SMA data. The calibrated data were then imaged and analyzed in a standard manner us-

² <https://lweb.cfa.harvard.edu/~cqj/mircook.html>

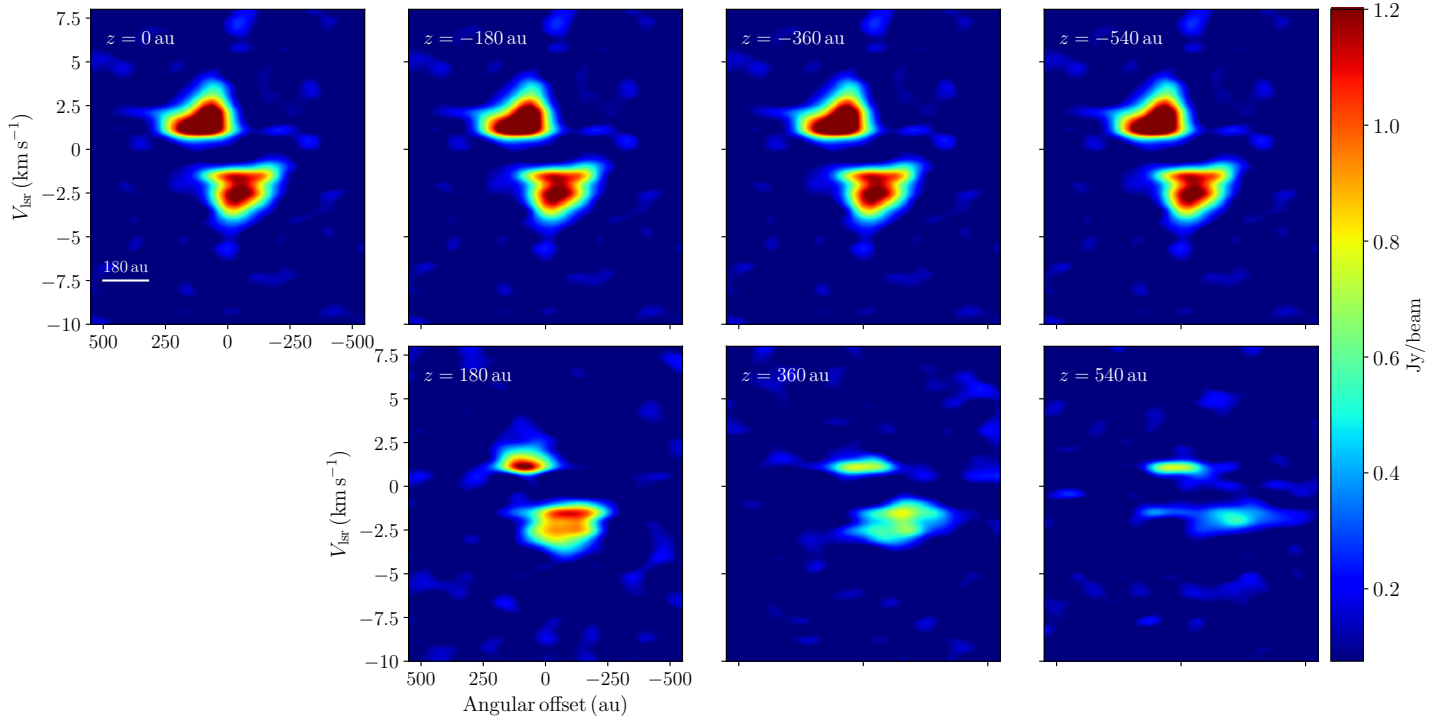


Figure 3. Position-velocity diagrams parallel to the disk mid-plane from the emission of the ^{12}CO ($J=2-1$) transition at different heights from $z = -540$ au to $z = 540$ au with an interval of 180 au. The vertical axes are the line of sight velocity with respect to the LSR velocity and the horizontal axes are the perpendicular distances with respect to the outflow axis. The color scale bar on the right side shows the intensity in Jy/Beam. The white bars indicate the angular resolution (140 au or $1''$) and velocity resolution (0.18 km s^{-1}) used for the position-velocity cuts.

ing Common Astronomy Software Applications (CASA) package. We also used some routines in Python to image the data (Astropy Collaboration et al. 2013). A 1.36 mm continuum image was obtained by averaging line-free channels in the lower sideband with a bandwidth of about 8 GHz. For this image, we used a robust factor of zero in order to obtain an optimal compromise between sensitivity and angular resolution. The continuum image *rms*-noise is $2.2 \text{ mJy beam}^{-1}$ at an angular resolution of $1.1'' \times 0.9''$ with a PA (Position Angle) of -85.8° . For the line image, we obtained a *rms*-noise of $90 \text{ mJy beam}^{-1} \text{ km s}^{-1}$ at an angular resolution of $1.2'' \times 0.96''$ with a PA of -85.5° . For the line image, we used a robust factor of 2.0 in order to obtain a better sensitivity. The resulting SMA rms in the channels maps is higher than that obtained in Launhardt et al. (2009), which is 20 mJy Beam^{-1} at an effective beam size of $1.47''$.

3. RESULTS

Figure 1 shows the moment zero map of the ^{12}CO ($J=2-1$) emission line overlaid in white contours of the 1.36 mm continuum map. This continuum emission is tracing the edge-on disk surrounding the young source CB26 (e.g., Stecklum et al. 2004; Sauter et al. 2009; Akimkin et al. 2012). The ^{12}CO ($J=2-1$) emission ex-

tends further out than the continuum emission along the southeast-northwest. We note that the extent of the molecular outflow is around ~ 1600 au, and the width is ~ 600 au. For the continuum emission, a Gaussian fit to the CB26 disk resulted in a deconvolved size of $196 \pm 31 \text{ au} \times 42 \pm 29 \text{ au}$ ($1.4'' \pm 0.1'' \times 0.3'' \pm 0.2''$) with position angle of $59^\circ \pm 3^\circ$, and an integrated flux of $161 \pm 8 \text{ mJy}$ together with a peak flux of 82 mJy Beam^{-1} . The phase center of CB26 disk is at $\alpha_{J2000.0} = 04^{\text{h}}59^{\text{m}}50^{\text{s}}.742$, and $\delta_{J2000.0} = +52^\circ 04' 43''.49$. The integrated flux is indeed lower to that estimated by Launhardt et al. (2009), which is 190 mJy . This could be explained as we are not recovering all the extended emission given that the effective beam size from Launhardt et al. (2009) is larger, $1.47''$. However, if we consider that the estimated uncertainty in the flux scale is between 15% to 20%, our integrated flux could increase to $193 \pm 10 \text{ mJy}$, a value is similar to the one estimated by them.

The first moment or the intensity weighted velocity map of the ^{12}CO ($J=2-1$) emission line is presented in Figure 2. We note that the east side of the molecular outflow presents blueshifted velocities, while the west side presents redshifted velocities. This difference of the velocities is proposed as rotation around the outflow axis (Launhardt et al. 2009). The inclination angle of this

source respect to the plane of the sky is $i = 5^\circ \pm 4^\circ$ (Launhardt et al. 2009), therefore, the lower edge of the outflow has an excess redshifted velocity. Consequently, the putative rotating outflow in CB26 is an excellent object to study the kinematics and nature of the flow.

Figure 3 presents the position-velocity diagrams of the emission from the molecular line of ^{12}CO ($J=2-1$). The different panels of this figure correspond to parallel cuts at different heights above the disk mid-plane, these cuts were made from $z=-540$ au to $z=540$ au with intervals of 180 au (these cuts correspond to the dashed lines in Figure 2). We note that all position-velocity diagrams present signatures of rotation, in a range of $\sim 1-3$ km s^{-1} . The position-velocity diagrams presented in this figure does not present a hollow structure, this might be explained as we do not have enough angular and spectral resolution to resolve angularly the outflow. This hollow structure is shown in other molecular outflows, e.g., Orion Source I (Hirota et al. 2017 and López-Vázquez et al. 2020) and HH 30 (Louvet et al. 2018). The apparent lack of molecular emission between ~ 1.5 km s^{-1} and 1 km s^{-1} observed in Figure 3, could be due to the missing flux of the large-scale structure of the envelope.

With the position-velocity diagrams presented in Figure 3, we can obtain information about the kinematic and physical properties of the molecular outflow because they show rotation and expansion signatures as will be described later. These properties are: the radius R , the expansion velocity v_{exp} , the rotation velocity v_{rot} , and additionally we obtain the opening angle θ_{opening} and the specific angular momentum j . These quantities, except for the specific angular momentum, are measured by a Gaussian fit to the intensity profile as a function of the radius or velocity, as appropriate. For more details see appendix of López-Vázquez et al. (2020) for the outflow in Orion Source I object. These measured quantities, the radius, the expansion, and the rotation velocities were not made for a height of $z = 0$ au, this is because the accretion disk is located at this height.

The left panel of Figure 4 shows the radius R from the molecular outflow as a function of the height z . We note that these radii, in lower edge ($z < 0$) of the molecular outflow, increase with the height above the disk mid-plane, however, this behavior is not evident in the upper edge $z > 0$ from this outflow. The radius is in a range of $\sim 180-280$ au, the error bars of these radii are obtained from the gaussian fit to the intensity profile as a function of the distance to the outflow axis. With these radii and for fixed centrifugal radius, $R_{\text{cen}} = 200$ au, this radius corresponds to the disk radius measurement by Launhardt et al. (2009), the opening angle can be defined as (see Figure 6 of López-Vázquez et al. 2020)

$$\theta_{\text{opening}} = \tan^{-1} \left(\frac{R - R_{\text{cen}}}{z} \right). \quad (1)$$

This angle is shown on the right panel of the Figure 4. Hirota et al. (2017) and López-Vázquez et al. (2020), measured this angle for the molecular outflow associated with Orion Source I, and they found that this angle decreases with the height above the disk mid-plane. In this source, the opening angle also decreases with the height above the disk and presents the same behavior that reported by the molecular outflow of Orion Source I (Hirota et al. 2017; López-Vázquez et al. 2020). This angle is in a range of $\sim 9-32^\circ$. The error bars are derived from the gaussian fit from the radii to the intensity profile. The fact that we used the centrifugal radius for our opening angle estimation is because this angle is a well indicator that the molecular outflow could close up at higher heights.

The left panel of Figure 5 presents the projected expansion velocity v_{exp} of the line of sight as a function of the height z . If we consider cylindrical coordinates, this velocity corresponds to the velocity in the radial direction (see Tabone et al. 2020). This velocity is in the range of $2-4$ km s^{-1} and increases with the height above the disk mid-plane, except for the height of $z=540$ au. Also, we can estimate the expansion velocity in the source system applying the correction $v_{\text{exp,source}} \sim v_{\text{exp}}/\cos i$, as the inclination angle respect to the plane of the sky is small ($\sim 5^\circ$), this results in an expansion velocity from the source system similar to the value of the projected expansion velocity. While, the rotation velocity as a function of the height is shown in the right panel of Figure 5. This velocity is in the range of $1-3$ km s^{-1} and decreases with the height above the disk mid-plane. The error bars are obtained from the gaussian fit to the intensity profile as a function of the velocity (see Appendix of López-Vázquez et al. 2020).

Figure 6 present the specific angular momentum j as a function of the height z . The specific angular momentum is calculated using the radius reported in left panel of Figure 4 as $j = Rv_{\text{rot}}$. The angular momentum decreases with the height. The specific angular momentum of the outflow is $\sim 200-700$ au km s^{-1} . The error bars are derived from the gaussian fits from the radii and rotation velocities to the intensity profile.

3.1. Mass of the outflow, the disk, and the central source

Assuming local thermodynamic equilibrium and that the ^{12}CO ($J=2-1$) molecular emission is optically thick, following the formalism of Zapata et al. (2014), the lower limit of the mass of the outflow is

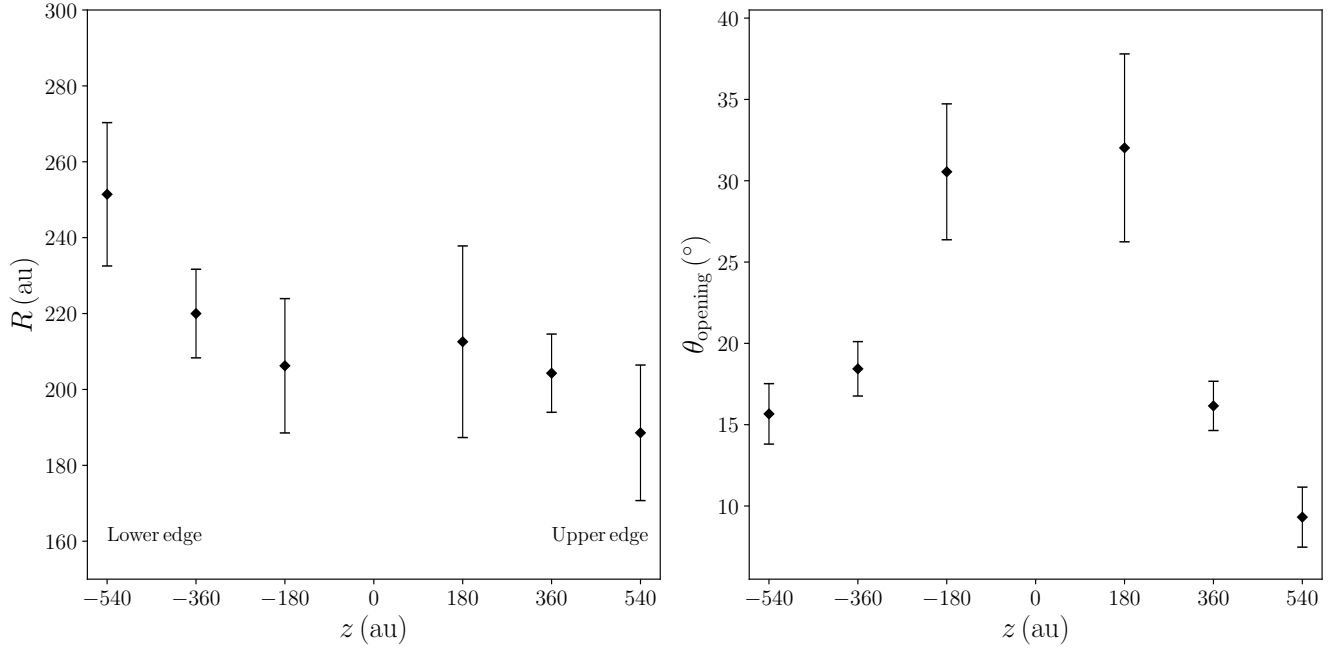


Figure 4. Left panel: the radius of the outflow R . Right panel: the opening angle of the outflow θ_{opening} . These values are derived from the position-velocity diagrams in Figure 3. The error bars are derived from the gaussian fit.

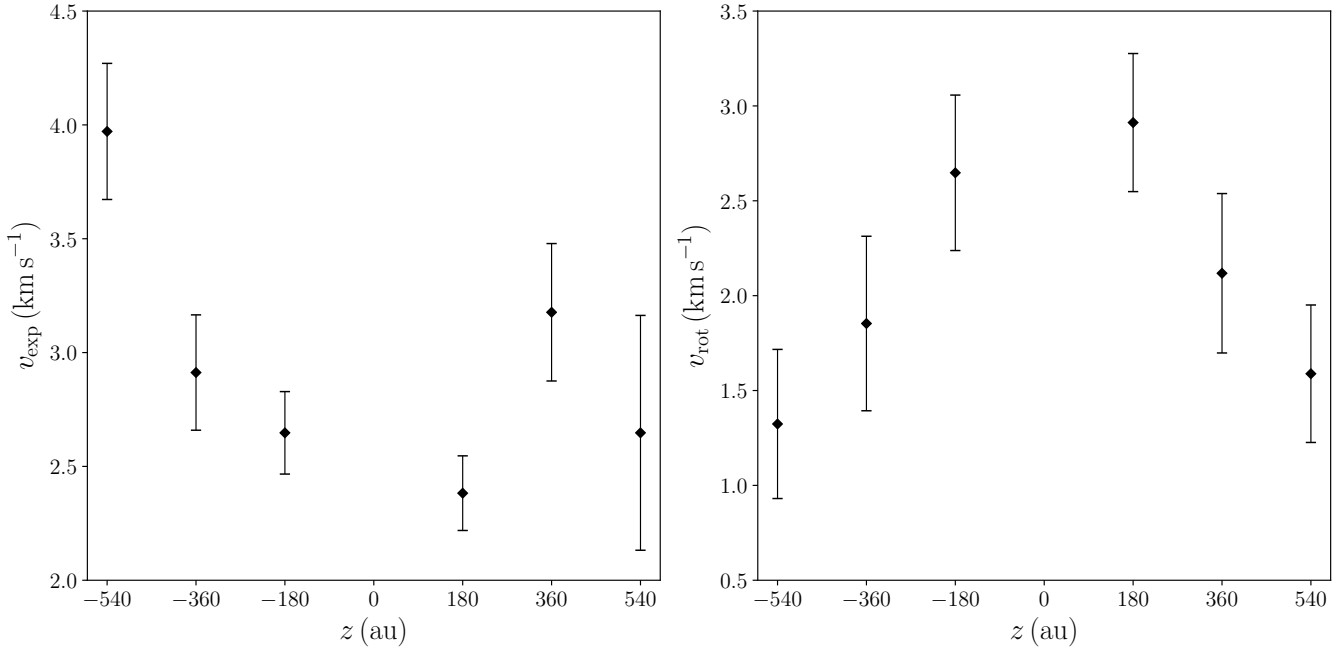


Figure 5. Left panel: the expansion velocity perpendicular to the outflow axis v_{exp} measured at the radius R . Right panel: the rotation velocity v_{rot} measured at the radius R . These values are derived from the position-velocity diagrams in Figures 3. The error bars are derived from the gaussian fit.

$$\times \left[\frac{\exp\left(\frac{5.53}{T_{\text{ex}}}\right)}{1 - \exp\left(\frac{-11.06}{T_{\text{ex}}}\right)} \right] \left[\frac{\int I_{\nu} dv}{\text{Jy km s}^{-1}} \right], \quad (2)$$

$$\left[\frac{M_{\text{H}_2}}{M_{\odot}} \right] = 1.2 \times 10^{-15} X_{\frac{\text{H}_2}{\text{CO}}} \left[\frac{\Delta\Omega}{\text{arcsec}^2} \right] \left[\frac{D}{\text{pc}} \right]^2$$

where $X_{\frac{\text{H}_2}{\text{CO}}}$ is the fractional abundance of ^{12}CO with respect to H_2 , for this source, we assumed an abundance

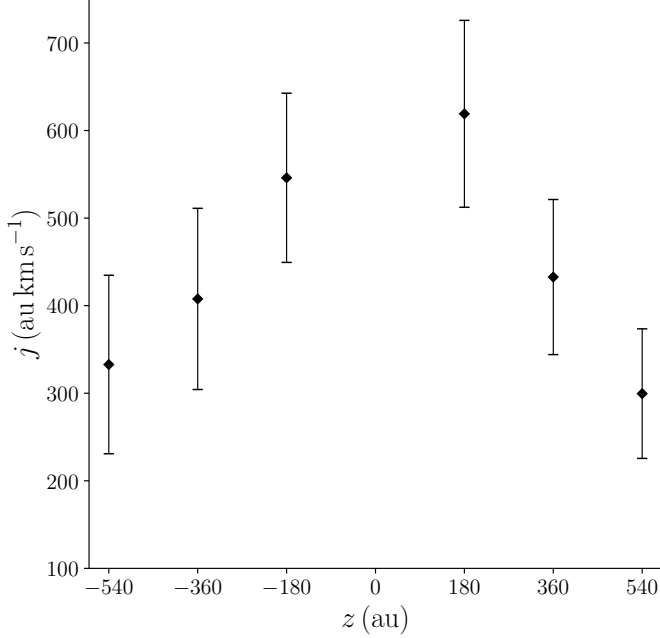


Figure 6. The specific angular momentum j as a function of the height z . The error bars are derived from the gaussian fit.

of 7.5×10^{-5} (Launhardt et al. 2009). The variable $\Delta\Omega$ is the solid angle of the source in arcsec², D is the distance in parsec (140 pc), I_ν is the intensity of the emission of ¹²CO in Jy, dv is the velocity range in km s⁻¹, and T_{ex} is the excitation temperature given by (Estalella & Anglada 1994):

$$\left[\frac{T_{\text{ex}}}{K}\right] = \frac{h\nu/k}{\ln\left(1 + \frac{h\nu/k}{T_a + J_\nu(T_{\text{bg}})}\right)} = \frac{11.07}{\ln\left(1 + \frac{11.07\text{K}}{T_a(^{12}\text{CO}) + 0.19\text{K}}\right)}, \quad (3)$$

where h is the Planck constant, k is the Boltzmann constant, ν is the rest frequency in GHz, $T_a = 16$ K is the observed antenna temperature given by the peak of the ¹²CO emission and $J_\nu(T_{\text{bg}})$ is intensity in units of temperature at the background temperature $T_{\text{bg}} = 2.7$ K. With this equation we obtain an excitation temperature of $T_{\text{ex}} \approx 21$ K. Using this temperature and the values mentioned above, we estimate a mass for the outflow powered by CB 26 of $M_{\text{outflow}} \sim 5 \pm 1.5 \times 10^{-5} M_\odot$. This value is lower by one order magnitude than the mass calculated by Launhardt et al. (2009). The difference between the mass obtained by us and the mass calculated by Launhardt et al. (2009) could be because there are uncertainties in the column density n_0 , and the kinetic gas temperature in the outflow T_0 (see section 4.2 of Launhardt et al. 2009). The discrepancy found in the outflow mass by the current work and the mass calculated by Launhardt et al. (2009), could be due to the difference between the fluxes.

On the other hand, now assuming that the dust emission is optically thin, and using the relationship of Hilde-

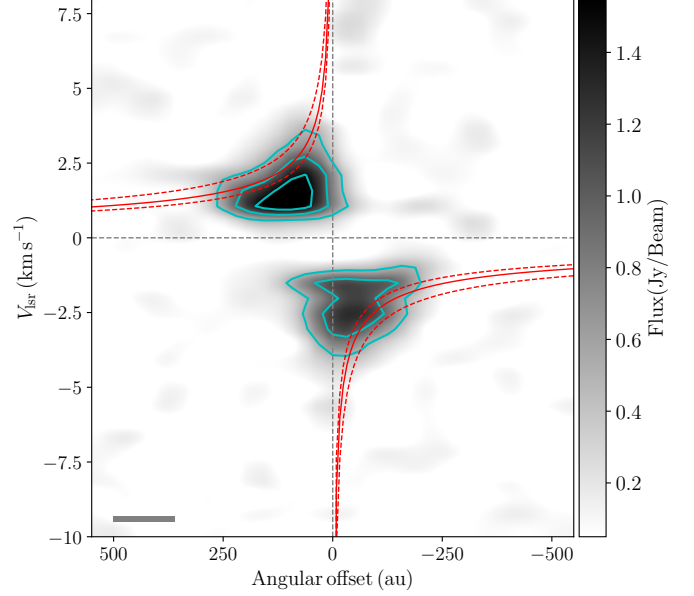


Figure 7. Position-velocity diagram of ¹²CO (J=2-1) over the disk mid-plane ($z=0$). The color scale bar on the right side shows the intensity in Jy/beam. The red solid line shows the Keplerian velocity profile surrounding $0.66 \pm 0.03 M_\odot$ central object. The gray bar represents the angular resolution (140 au or 1'') and velocity resolution (0.18 km s^{-1}) used for the position-velocity cut. Contours levels start from 5σ in steps of 5σ , where 1σ is $0.1012 \text{ Jy beam}^{-1}$.

brand (1983), the dust mass of the protoplanetary disk is

$$M_d = \frac{F_\nu D^2}{\kappa_\nu B_\nu(T_d)} \simeq 9.8 \pm 0.4 \times 10^{-7} \left(\frac{F_\nu}{\text{mJy}}\right) \left(\frac{D}{100\text{pc}}\right)^2 M_\odot \quad (4)$$

where F_ν is the mm flux, D is the distance to the source, T_d is the dust temperature, B_ν is the Planck function at T_d , and κ_ν is the dust grain opacity. We use standard assumptions for the values of the parameters $T_d = 20$ K (Andrews & Williams 2005), and a power-law opacity of the form $\kappa_\nu = 10(\nu/1000 \text{ GHz})^\beta \text{ cm}^2 \text{ g}^{-1}$, with a β value of 1.1 ± 0.27 (Sauter et al. 2009). Using the above equation, we found a dust mass of $M_{\text{dust}} = 0.00031 \pm 0.00015 M_\odot$, so taking a typical ratio between the gas and dust in the ISM of 100, we obtain a total mass for the disk of $0.031 \pm 0.015 M_\odot$.

In order to estimate the dynamical mass of the central object, we fit a Keplerian velocity profile to the position-velocity diagram of the disk ($z=0$ au), this fit is shown in Figure 7. The best fit (red line), corresponds to a dynamical mass of $M_{\text{dyn}} = 0.66 \pm 0.03 M_\odot$ while the dashed lines are 1.0 (outer lines) and $0.5 M_\odot$ (inner lines), the best fit corresponds to the visual fit of a Keplerian curve $v_k = \sqrt{GM_{\text{dyn}}/r}$ where v_k and r are measured at the contours corresponding to the emission of 10σ of Figure

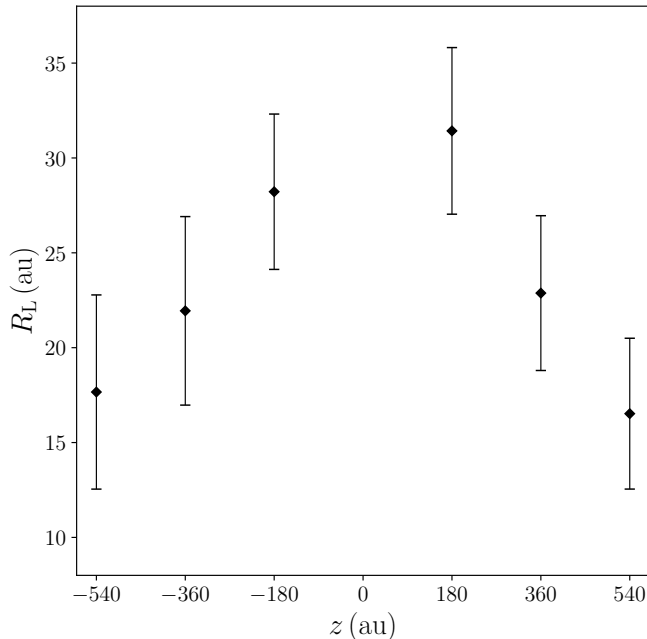


Figure 8. The launching radii R_L as a function of the height z . These radii are calculated solving the eq. (4) of Anderson et al. (2003) (see text). The error bars are derived from the gaussian fit.

7.

3.2. Origin of the molecular outflow

As mentioned in section 1, the origin of the molecular outflow is uncertain. A possibility is that the wind is launched through magneto-centrifugal processes from a rotating protostellar disk and then accelerated and collimated by magnetohydrodynamic forces. Under this scenario, we can calculate the launching radius following the equation (4) of Anderson et al. (2003) given by

$$\varpi_\infty v_{\phi,\infty} \Omega_0 - \frac{3}{2} (GM_*)^{2/3} \Omega_0^{2/3} - \frac{v_{p,\infty}^2 + v_{\phi,\infty}^2}{2} \approx 0, \quad (5)$$

where ϖ_∞ is the observed radial distance to the flow axis, in our case is R for each z , $v_{\phi,\infty}$ and $v_{p,\infty}$ are the toroidal and poloidal velocities observed at radius R . For this object, the toroidal velocity corresponds to the rotation velocity v_{rot} , while the outward velocity of the molecular outflow is $v_r \sim 10 \text{ km s}^{-1}$ (Launhardt et al. 2009), the outflow inclination angle is $i = 5^\circ \pm 4^\circ$, thus, the corrected outward velocity is $v_z = v_r / \cos i \sim 10.04 \pm 0.06 \text{ km s}^{-1}$, and the poloidal velocity is $v_p = \sqrt{v_z^2 + v_{\text{exp}}^2}$. The gravitational constant is G and the mass of the central protostar is M_* , we assume $M_* = 0.6 M_\odot$, a similar value to that estimated in Zhang et al. (2021). Finally, Ω_0 is the angular speed at the launching radius, given by

$$\Omega_0 = \left(\frac{GM_*}{\varpi_0^3} \right)^{1/2}, \quad (6)$$

where ϖ_0 is the launching radius R_L .

Solving Eq. (5) for R_L with the values mentioned above, we calculate the launching radius of the molecular outflow, this radius is shown as a function of the height above the disk mid-plane in Figure 8. We note that these radii (in a range of $\sim 15\text{--}35 \text{ au}$) decreases with the height.

4. DISCUSSION

Figures 4–6 show the structure and kinematic of the molecular outflow associated with CB 26. One can note that the radius, the opening angle, and the rotation velocity have a similar behavior to other rotating molecular outflows, *e.g.*, Orion Source I (Hirota et al. 2017 and López-Vázquez et al. 2020), HH 30 (Louvet et al. 2018), and NGC 1333 IRAS 4C (Zhang et al. 2018), this means that the radius increase with the height above the disk mid plane, and the opening angle and the rotation velocity decreases with the height above the disk mid-plane. With respect to the specific angular momentum, it seems to have the same behavior to the sources mentioned above, this is, it decreases with the height. In summary, a disk-wind driving the outflow could explain all the observed characteristics.

The masses estimated for the molecular outflow, $5 \pm 1.5 \times 10^{-5} M_\odot$, the protostellar disk, 0.06 ± 0.017 , and the central star, $\sim 0.6 \pm 0.03 M_\odot$, are all consistent with the values of the literature (*e.g.*, Launhardt et al. 2009; Zhang et al. 2021).

In section 3.2 we estimated the launching radius of the wind under assumption that the origin of the molecular outflow is the large radius of the Keplerian disk. This wind can be ejected by magneto-centrifugal mechanism or by photoevaporated disk wind. Nevertheless, Zapata et al. (2015) showed that magnetocentrifugal and photoevaporated disk winds do not have enough mass to account for the observed mass rates in the molecular outflow of DG Tau B, their argument is based on the assumption that the mass-loss rate of the wind is a fraction $f \sim 0.1$ of the mass accretion rate, $\dot{M}_w \sim f \dot{M}_{\text{d,a}}$. However, we note that recent ALMA observations for DG Tau B (de Valon et al. 2020) reported a lower outflow mass (a factor of 30), and suggested that a disk-wind could be responsible for the rotating outflow, however it still being massive to explain the outflow from DG Tau B.

In particular this source has an outflow mass of $5 \times 10^{-5} M_\odot$ (see section 3.1), for a corrected outward velocity $v_z \sim 10.04 \pm 0.06 \text{ km s}^{-1}$ and a projected size (diameter) of $z \sim 540 \text{ au}$, the kinematic time is $t_{\text{kin}} \sim 255 \pm 1.6 \text{ yr}$. Then, the molecular outflow mass loss rate is $\dot{M}_{\text{outflow}} = M_{\text{outflow}} / t_{\text{kin}} \sim 2 \pm 0.012 \times 10^{-7} M_\odot \text{ yr}^{-1}$, its linear momentum rate $\dot{P}_{\text{outflow}} = \dot{M}_{\text{outflow}} v_p \sim 2 \pm 0.035 \times 10^{-6} M_\odot \text{ yr}^{-1} \text{ km s}^{-1}$ or a height of $z = 540 \text{ au}$ its angular momen-

Table 1. Derived quantities of the molecular outflow and disk.

Parameter	Symbol	Value
Outflow mass	M_{outflow}	$5 \pm 1.5 \times 10^{-5} M_{\odot}$
Outflow mass loss rate	\dot{M}_{outflow}	$2 \pm 0.6 \times 10^{-7} M_{\odot} \text{ yr}^{-1}$
Outflow linear momentum rate	\dot{P}_{outflow}	$2 \pm 0.7 \times 10^{-6} M_{\odot} \text{ yr}^{-1} \text{ km s}^{-1}$
Outflow angular momentum rate	\dot{L}_{outflow}	$6 \pm 2.4 \times 10^{-5} M_{\odot} \text{ yr}^{-1} \text{ au km s}^{-1}$
Disk mass	M_d	$0.031 \pm 0.015 M_{\odot}$
Dynamical mass (central object)	M_{dyn}	$0.66 \pm 0.03 M_{\odot}$

tum rate is $\dot{L}_{\text{outflow}} = \dot{M}_{\text{outflow}} R v_{\text{rot}} \sim 6 \pm 1.5 \times 10^{-5} M_{\odot} \text{ yr}^{-1} \text{ au km s}^{-1} = 9 \pm 2.4 \times 10^3 M_{\odot} \text{ yr}^{-1} \text{ km}^2 \text{ s}^{-1}$. These estimated rates, as well as the outflow mass, the disk mass, and the dynamical mass of the central object are shown in Table 1.

If we take a value for the mass-loss rate for a disk-wind of $\dot{M}_{\text{wind}} \sim 10^{-7} M_{\odot} \text{ yr}^{-1}$, which is a higher value than that reported in DG Tau B, a Class I/II object, see Zapata et al. (2015). The expected mass-loss rate is thought to increase in younger objects, so this assumption should be reasonable. Thus, the linear momentum rate for the slow disk-wind is $\dot{P}_w = \dot{M}_w v_p \sim 1 \pm 0.014 \times 10^{-6} M_{\odot} \text{ yr}^{-1} \text{ km s}^{-1}$, and the angular momentum rate is $\dot{L}_w = \dot{M}_w r v_{\phi} = 3 \pm 0.7 \times 10^{-5} M_{\odot} \text{ yr}^{-1} \text{ au km s}^{-1} = 4.5 \pm 1.1 \times 10^3 M_{\odot} \text{ yr}^{-1} \text{ km}^2 \text{ s}^{-1}$. Both rates are very similar to the ones obtained to the molecular outflow in CB26 (\dot{P}_{outflow} and \dot{L}_{outflow}), which indicates that a disk-wind has enough momentum to drive the molecular outflow.

If the outflow is a disk wind, $\dot{M}_{\text{outflow}} = \dot{M}_w \sim f \dot{M}_{\text{d,a}}$, we can estimate the accretion luminosity at the stellar surface as

$$L_a = \eta \frac{GM_* \dot{M}_{\text{d,a}}}{R_*}, \quad (7)$$

where G is the gravitational constant (as above), M_* is the stellar mass, R_* is the stellar radius, and $\eta \sim 0.5$. Assuming $M_* = 0.6 M_{\odot}$ and $R_* = 2 R_{\odot}$ (Zhang et al. 2021), the accretion luminosity is $L_a \geq (1/f) 0.9 L_{\odot}$. This value is consistent to the reported value of the central source $L_* = 0.92 L_{\odot}$ (Zhang et al. 2021) by a factor of $f \sim 1$.

In summary, all the presented observational characteristics argue in favor of having a disk-wind in CB26 outflow. The disk-wind for this case has enough mass to account to the mass rates.

5. CONCLUSIONS

In this work, we present the SMA archive observations for the line emission of ^{12}CO ($J=2-1$) from the molecular outflow CB 26. Our main results are:

1. We find that the radius R (in a range of ~ 180 – 280 au) and the expansion velocity (in a range of 2 – 4

km s^{-1}) increase with the height above the disk mid-plane in lower edge of the molecular outflow ($z < 0$ au), however, this behavior is not evident in the upper edge ($z > 0$ au).

2. We find that the rotation velocity (in a range of 1 – 3 km s^{-1}), the specific angular momentum (in a range of 200 – 700 au km s^{-1}), and the launching radius (in a range of 15 – 35 au), decrease with the height above the disk mid-plane, as observed in other molecular rotating outflows.
3. We estimated the mass of the molecular outflow, $5 \pm 1.5 \times 10^{-5} M_{\odot}$, the mass of the accretion disk, $0.031 \pm 0.015 M_{\odot}$, and the mass of the central star $0.66 \pm 0.03 M_{\odot}$.
4. Estimations of the outflow linear momentum rate, the outflow angular momentum rate, and the accretion luminosity seem to be well explained by a disk-wind present in CB26.

REFERENCES

- Akimkin, V. V., Pavlyuchenkov, Y. N., Launhardt, R., et al. 2012, *Astronomy Reports*, 56, 915
- Anderson, J. M., Li, Z.-Y., Krasnopolsky, R., & Blandford, R. D. 2003, *ApJL*, 590, L107
- Andrews, S. M. & Williams, J. P. 2005, *ApJ*, 631, 1134. doi:10.1086/432712
- Astropy Collaboration, Robitaille, T. P., Tollerud, E. J., et al. 2013, *A&A*, 558, A33.
- Bachiller, R. 1996, *ARA&A*, 34, 111. doi:10.1146/annurev.astro.34.1.111
- Bai, X.-N., & Stone, J. M. 2017, *ApJ*, 836, 46
- Bai, X.-N., Ye, J., Goodman, J., et al. 2016, *ApJ*, 818, 152. doi:10.3847/0004-637X/818/2/152
- Blandford, R. D. & Payne, D. G. 1982, *MNRAS*, 199, 883. doi:10.1093/mnras/199.4.883
- Bjerkeli, P., van der Wiel, M. H. D., Harsono, D., et al. 2016, *Nature*, 540, 406. doi:10.1038/nature20600
- Booth, A. S., Tabone, B., Ilee, J. D., et al. 2021, *ApJS*, 257, 16. doi:10.3847/1538-4365/ac1ad4
- de Valon, A., Dougados, C., Cabrit, S., et al. 2020, *A&A*, 634, L12. doi:10.1051/0004-6361/201936950
- Estalella, R., Anglada, G. 1994, ISBN 84-8338-098-6
- Hildebrand, R. H. 1983, *QJRAS*, 24, 267
- Hirota, T., Machida, M. N., Matsushita, Y., et al. 2017, *Nature Astronomy*, 1, 0146

- Launhardt, R., Pavlyuchenkov, Y., Gueth, F., et al. 2009, *A&A*, 494, 147
- Launhardt, R., Stutz, A. M., Schmiedeke, A., et al. 2013, *A&A*, 551, A98. doi:10.1051/0004-6361/201220477
- Lee, C.-F., Hirano, N., Palau, A., et al. 2009, *ApJ*, 699, 1584. doi:10.1088/0004-637X/699/2/1584
- Lee, C.-F., Ho, P. T. P., Li, Z.-Y., et al. 2017, *Nature Astronomy*, 1, 0152. doi:10.1038/s41550-017-0152
- Lee, C.-F., Li, Z.-Y., Codella, C., et al. 2018, *ApJ*, 856, 14. doi:10.3847/1538-4357/aaae6d
- López-Vázquez, J. A., Cantó, J., & Lizano, S. 2019, *ApJ*, 879, 42
- López-Vázquez, J. A., Zapata, L. A., Lizano, S., et al. 2020, *ApJ*, 904, 158. doi:10.3847/1538-4357/abbe24
- Louvet, F., Dougados, C., Cabrit, S., et al. 2018, *A&A*, 618, A120
- Machida, M. N. 2014, *ApJL*, 796, L17. doi:10.1088/2041-8205/796/1/L17
- Matsushita, Y., Takahashi, S., Ishii, S., et al. 2021, *ApJ*, 916, 23. doi:10.3847/1538-4357/ac069f
- Pech, G., Zapata, L. A., Loinard, L., et al. 2012, *ApJ*, 751, 78. doi:10.1088/0004-637X/751/1/78
- Pety, J., Gueth, F., Guilloteau, S., et al. 2006, *A&A*, 458, 841. doi:10.1051/0004-6361/20065814
- Pudritz, R. E. & Norman, C. A. 1986, *ApJ*, 301, 571. doi:10.1086/163924
- Ray, T. P. & Ferreira, J. 2021, *New A Rev.*, 93, 101615. doi:10.1016/j.newar.2021.101615
- Sauter, J., Wolf, S., Launhardt, R., et al. 2009, *A&A*, 505, 1167
- Shu, F., Najita, J., Galli, D., et al. 1993, *Protostars and Planets III*, 3
- Shu, F. H., Ruden, S. P., Lada, C. J., et al. 1991, *ApJL*, 370, L31. doi:10.1086/185970
- Stecklum, B., Launhardt, R., Fischer, O., et al. 2004, *ApJ*, 617, 418
- Tabone, B., Cabrit, S., Pineau des Forêts, G., et al. 2020, *A&A*, 640, A82. doi:10.1051/0004-6361/201834377
- Ulrich, R. K. 1976, *ApJ*, 210, 377
- Wang, L., Bai, X.-N., & Goodman, J. 2019, *ApJ*, 874, 90
- Zapata, L. A., Arce, H. G., Brassfield, E., et al. 2014, *MNRAS*, 441, 3696
- Zapata, L. A., Lizano, S., Rodríguez, L. F., et al. 2015, *ApJ*, 798, 13
- Zapata, L. A., Schmid-Burgk, J., Muders, D., et al. 2010, *A&A*, 510, A2. doi:10.1051/0004-6361/2008102451
- Zhang, Y., Higuchi, A. E., Sakai, N., et al. 2018, *ApJ*, 864, 76
- Zhang, C.-P., Launhardt, R., Liu, Y., et al. 2021, *A&A*, 646, A18. doi:10.1051/0004-6361/202039536